DR2004092

Data Repository Material (Text and Table)

Description of data, processing, inversions and modeling

The interferograms (see Table DR1) were processed using the Jet Propulsion Lab/Caltech ROI_pac software (Rosen, 2004). The synthetic aperture radar (SAR) images were acquired by the ERS-1 and ERS-2 satellites (56.6 mm radar wavelength). We used digital terrain elevation data with a three-arcsecond posting to remove the topographic component of the differential interferograms (#1-3 in Table DR1) and to calibrate the digital elevation model (DEM) derived from with the ERS-1/ERS-2 Tandem pair (interferogram #4) (Bürgmann et al., 2000; Rosen et al., 2000). The perpendicular components of the interferometric baselines vary between the interferograms and results in different sensitivity to elevation, expressed as ambiguity height (the elevation change that causes one fringe of phase) in Table DR1.

We processed the Tandem pair of ERS SAR images (Table DR1, #4) for the Shahdad area, with a one-day time separation, to make a DEM. We differentially processed the co-seismic interferograms with three different elevation models: the 3-arcsecond alone, the Tandem DEM alone, and the combination. All show the same Shahdad range change pattern, so the Shahdad feature is not due to an error in the elevation models. The interferograms were processed with 4 range and 20 azimuth looks to produce ~80 m pixels. We used a power spectrum filter to smooth the results (Goldstein and Werner, 1998). The ERS satellites on descending orbits look to the right (west) at an angle of 23° from the vertical at the center of the swath. The look azimuth varies with latitude and is approximately 78.5 degrees west of North for this scene. The interferogram measures only the component of range change in the radar line-of-sight.

The best-fit model for the Fandoqa earthquake was determined using a non-linear hybrid Monte-Carlo / downhill simplex inversion algorithm (Wright et al., 1999) that minimizes the square misfit between the observed surface range changes and those predicted by a dislocation in an elastic half space (Okada, 1985). We sampled the average of the unwrapped phase of interferograms 1 and 2 (Table DR1) on a 1 km grid within about 10 km of the mainshock rupture and on a 4 km grid elsewhere (see Figure DR1). The simple, 1-fault, constant-slip model provides a good fit to the data (rms residual = 11 mm) except near the ends of the fault. We used linear elastic Lamé constants $=33.6$ GPa and $=33.6$ GPa, corresponding to a Poisson ratio $=0.25$. All ten dislocation-rectangle parameters were allowed to vary in the inversion except the depth to the top of the fault rupture, which was fixed to zero. Dislocation patch parameters are: strike 152°, dip 60°, rake –167°, slip 1.7 m, patch length 25.7 km, width 7.7 km, depth to bottom of fault 6.7 km, and projected center at surface 565.1 km E, 3321.9 km N in UTM zone 40. The moment of the solution is 11.2×10^{18} N-m and $M_w=6.6$. The surface deformation from this model is shown in Fig. 2B of the main paper.

More complex fault models for the Fandoqa earthquake do not significantly influence the phase changes observed in the Shahdad fold-and-thrust belt since it is at least 8 km to the east. The above process was repeated to find the best fit single fault for the Shahdad thrust by holding the Fandoqa dislocation fixed and fitting the average of the two interferograms, except that the data distribution was densified around the Shahdad thrust to a 1 km grid, with a 4 km grid elsewhere (see Figure DR2). This is equivalent to fitting the difference between the interferogram and the Fandoqa solution as shown in Fig. 2C. The single look direction that is nearly perpendicular to the strike of the structures in the Shahdad fold-and-thrust belt means that the interferograms are very insensitive to strike-slip components of slip on those structures. For this reason, the rake was fixed at 90° to invert for only the dip-slip component. The best-fitting rectangular

dislocation had a strike of 151°, dip 9.7°, slip 0.070 m, length 28.9 km, width 22.2 km, depth to

top 0.8 km, depth to bottom 4.6 km, and center of projection to the surface at 602.2 km E, and

3328.4 km N (UTM40). The moment of the solution is 1.5×10^{18} N-m and M_w=6.1. The fit RMS

residual is 6 mm including the Fandoqa rupture and the Shahdad basal thrust slip. The analytic

solutions for strain due to a dislocation (Okada, 1985, 1992) only apply to an elastic half-space

with no surface topography. Because the SAR measures displacements at the topographic surface

(sloping about 2.6°), we adjust the model dislocation to be at the true depth below the local

surface elevation (Williams and Wadge, 1998), as shown on Fig. 1B. After this adjustment the

modeled Shahdad basal thrust has a dip of 6.1° relative to horizontal.

To determine the distribution of slip on the Shahdad basal thrust fault, we extended the best-fit

uniform slip fault patch in all directions to form a 32 x 60 km plane. This extended fault was

divided into 4 x 4 km patches and an inversion was carried out to determine the best-fit positive

slip distribution using the Fast Non-Negative Least Squares algorithm (Bro and De Jong, 1997).

As described above, the InSAR data is relatively insensitive to the orientation of the slip vector

on the Shahdad thrust (provided there is some component towards the satellite), we assumed

pure thrust motion on the basal thrust. To remove unnecessary short-wavelength oscillations in

the best-fit solution, we simultaneously followed the common practice of minimizing the slip

roughness, as defined by the finite-difference approximation of the Laplacian operator (e.g.,

Harris and Segall, 1987). The relative importance of the smoothing operator was adjusted to find

the smoothest solution that provided a satisfactory fit to the data (Figure DR3). The final solution

(Figure DR3B) reduces the RMS misfit to 5 mm.

Errors in the slip distribution were estimated with a Monte Carlo simulation, using the noise

function derived from the average interferogram in the far away from the deformation (Wright et

al., 2003). The errors, shown in Fig. DR4, were determined for each of the 4 x 4 km patches shown in Figs. 3 and DR3.

The three-dimensional boundary element code Poly3D (Thomas, 1993) is based upon the governing equations of linear elasticity and the displacement discontinuity method (Crouch and Starfield, 1983). Triangular dislocation elements are constructed via the superposition of three angular dislocation solutions (Comninou and Dunders, 1975). Within each triangle, the dislocation is constant. Multiple triangular elements compose a 3-D fault surface. The faults are embedded in a homogeneous, isotropic elastic half-space. The magnitudes of the displacement discontinuity (slip) on the faults can be prescribed, as it is for the Fandoqa rupture in our model, or can be computed to satisfy prescribed traction boundary conditions on the fault(s). In our model, we prescribe a zero shear traction boundary condition to the Shahdad basal thrust and splay faults. In this manner, the Shahdad faults can be considered as slipping without friction in response to the static stress perturbation produced by slip on the Fandoqa fault or at least completely releasing the applied stress change. Once displacement discontinuities (slip distribution) on the faults are determined, displacements at the ground surface can be calculated.

The final Poly3D boundary element model used a rectangular plane for the Shahdad basal thrust that is the same length as the one used in the distributed slip inversion, but limited in the width direction to the same 22 km as the simple, constant-slip inversion solution. Extending the Shahdad basal thrust closer to the surface or deeper resulted in surface deformation that was drastically different from the InSAR observations. Four splay faults were added to the Poly3D model as curved surfaces that project to the surface on the front edges of the folds mapped on Landsat images and the digital topography (shown as faults on the Figs. 1 and 2 of the main paper). The splays have a dip of 30° to the southwest down to the Shahdad basal thrust and

terminate at a depth of 1 km, except for the northern part of the frontal splay on the NE that

extends to the surface (see Figure DR5).

TABLE DR1. PARAMETERS OF RADAR IMAGES USED IN THE INTERFEROMETRIC

ANALYSIS.

Interferogram	Start date	End date	Ambiguity height (m)
1	1996/5/27	1998/9/14	130
2	1996/4/22	1999/4/12	250
3	1998/9/14	1999/3/8	130
4	1996/5/26	1996/5/27	80

References and notes:
Bro, R., and De Jong, S., 1997, J. Chemometrics, v. 11, p. 392-401.
Bürgmann, R., Rosen, P.A., and Fielding, E.J., 2000, Synthetic aperture radar interferometry to measure Earth's surface topography and its deformation: Annual Review of Earth and Planetary Sciences, v. 28, p. 169-209.
Comninou, M.A., and Dunders, J., 1975, The angular dislocation in a half-space: Journal of Elasticity, v. 5, p. 203-216.
Crouch, S.L., and Starfield, A.M., 1983, Boundary Element Methods in Solid Mechanics: London, Allen and Unwin.
Goldstein, R.M., and Werner, C.L., 1998, Radar interferogram filtering for geophysical applications: Geophysical Research Letters, v. 25, no. 21, p. 4035-4038.
Harris, R.A., and Segall, P., 1987, Journal of Geophysical Research, v. 92, p. 7945-7962.
Okada, Y., 1985, Surface deformation due to shear and tensile faults in a half-space: Bulletin Of the Seismological Society Of America, v. 75, no. 4, p. 1135-1154.
—, 1992, Internal deformation due to shear and tensile faults in a half-space: Bulletin Of the Seismological Society Of America, v. 82, no. 2, p. 1018–1040.
Rosen, P., 2004, Updated repeat orbit interferometry package released: Eos, Transactions, American Geophysical Union, v. 85, no. 5, p. 47.
Rosen, P.A., Hensley, S., Joughin, I.R., Li, F.K., Madsen, S.N., Rodriguez, E., and Goldstein, R.M., 2000, Synthetic aperture radar interferometry: Proceedings of the IEEE, v. 88, no. 3, p. 333-382.
Thomas, A.L., 1993, Poly3D: a three-dimensional, polygonal element, displacement discontinuity boundary element computer program with applications to fractures, faults, and cavities in the Earth's crust [M.Sc. thesis]: Stanford, California, USA, Stanford University, 221 p.
Williams, C.A., and Wadge, G., 1998, The effects of topography on magma chamber deformation models: Application to Mt Etna and radar interferometry: Geophysical Research Letters, v. 25, no. 10, p. 1549-1552.
Wright, T.J., Lu, Z., and Wicks, C., 2003, Source model for the M_w 6.7, 23 October 2002, Nenana Mountain Earthquake (Alaska) from InSAR: Geophysical Research Letters, v. 30, no. 18, p. 1974, doi:10.1029/2003GL018014.
Wright, T.J., Parsons, B.E., Jackson, J.A., Haynes, M., Fielding, E.J., England, P.C., and Clarke, P.J., 1999, Source parameters of the 1 October 1995 Dinar (Turkey) earthquake from

SAR interferometry and seismic bodywave modelling: Earth and Planetary Science Letters, v. 172, no. 1-2, p. 23-37.

Figure legends

Figure DR1: Sampling of average interferogram used for Fandoqa rupture inversion: 1x1 km near fault, 4x4 km spacing elsewhere. Coordinates are UTM zone 40 kilometers, range change shown as colors in meters.

Figure DR2. Interferogram sampling for Shahdad slip inversions. Red lines show projection of Fandoqa and Shahdad basal thrust to surface. Range change after subtracting Fandoqa mainshock model in meters shown as colors.

Figure DR3. Distributed slip solutions for Shahdad basal thrust, with three different smoothing factors. A) Smoothing factor 100 (strong smoothing), B) smoothing factor 25 (same as Fig. 3), C) smoothing factor 0 (no smoothing). Slip in meters.

Figure DR4. Estimated errors for the distributed slip solutions, in meters, from Monte Carlo simulation using errors from average interferogram area away from earthquake deformation.

Figure DR5. Geometry of splay faults used in Poly3D, with surface faults (black). Average interferogram of Fig. 2C is shown as partially transparent with splay faults visible beneath in blue-yellow shading. Fandoqa main-shock rupture plain is also shown in shading. Surface projection of Shahdad basal thrust is thin black line. Area is the same as Figs. 2C and 2D and labeled coordinates are UTM zone 40 meters.
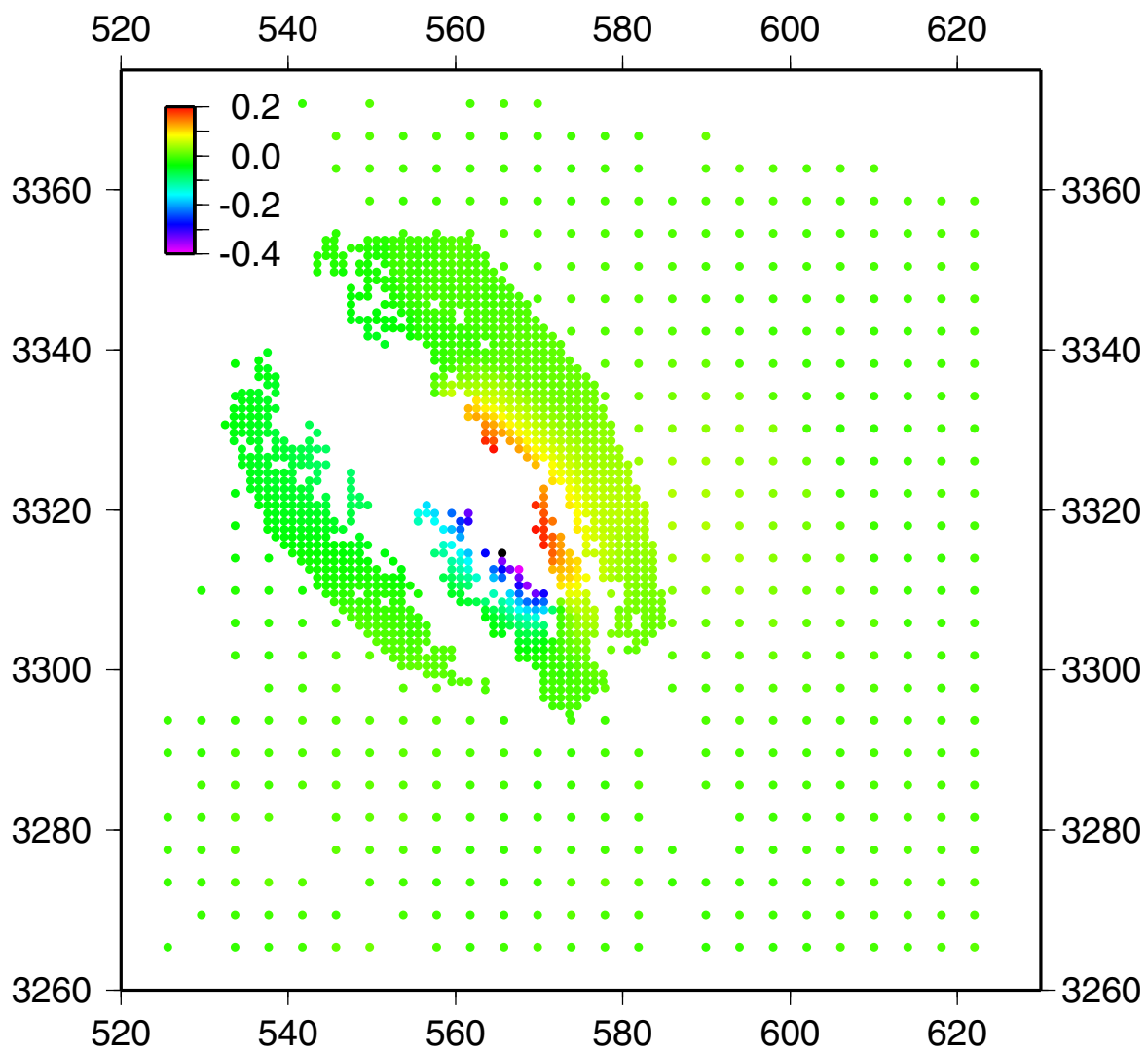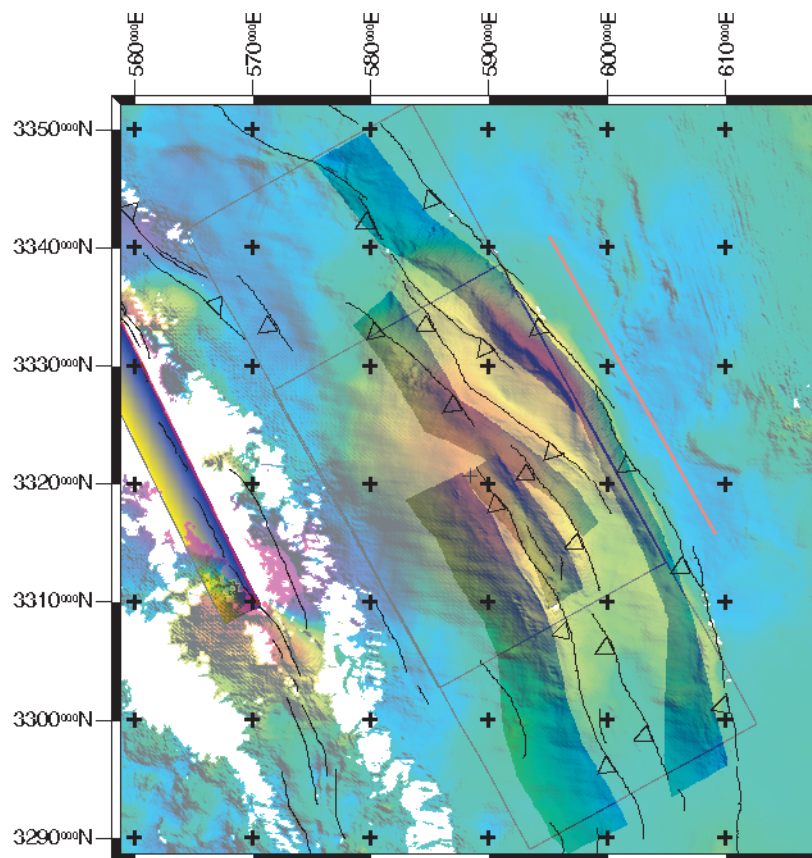
Fielding et al., Figure DR1

Fielding et al., Figure DR2
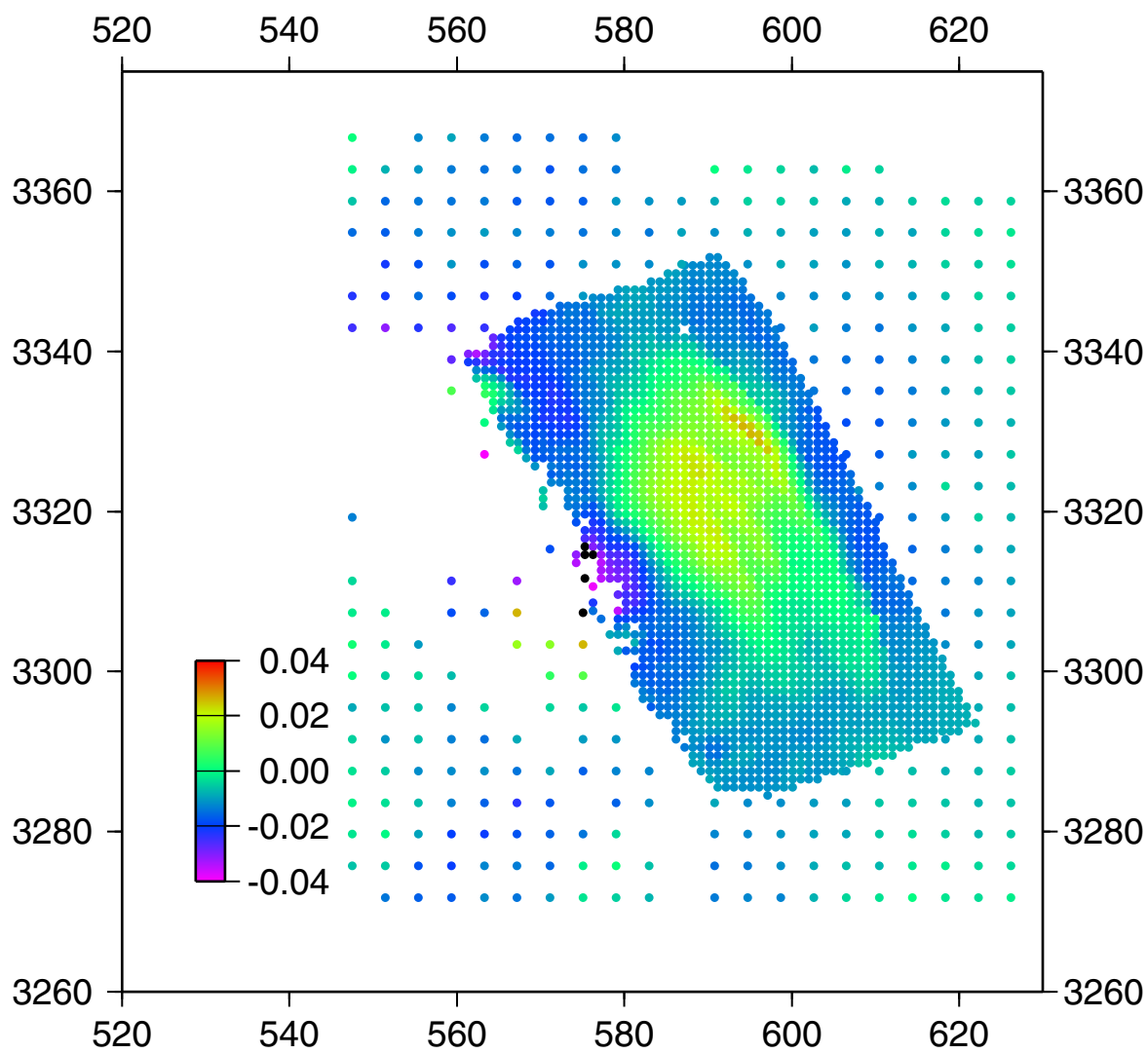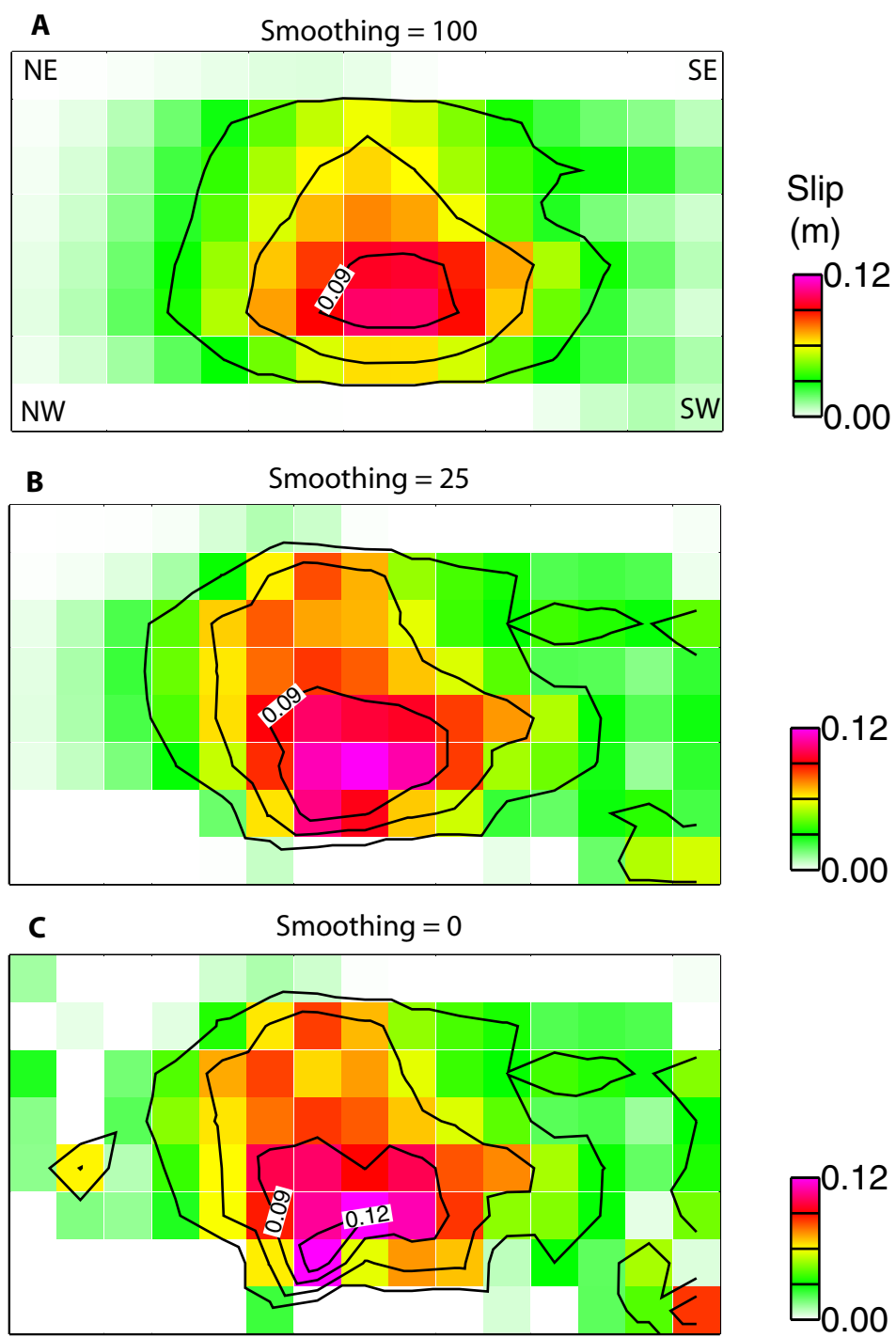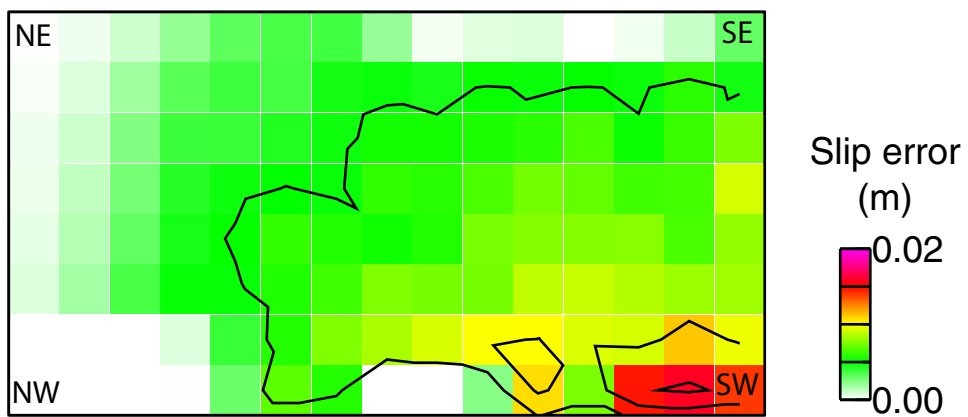
Fielding et al., Figure DR4

Fielding et al., Figure DR5